LA-UR-18-28325 (Accepted Manuscript)

Spatial transport of runaway electrons in axisymmetric tokamak plasmas

McDevitt, Christopher Joseph
Guo, Zehua
Tang, Xianzhu

To be published in: Plasma Physics and Controlled Fusion

DOI to publisher's version: 10.1088/1361-6587/aaf4d1

Permalink to record: http://permalink.lanl.gov/object/view?what=info:lanl-repo/lareport/LA-UR-18-28325

Spatial Transport of Runaway Electrons in Axisymmetric Tokamak Plasmas

Christopher J. McDevitt, Zehua Guo, and Xian-Zhu Tang

Theoretical Division, Los Alamos National Laboratory, Los Alamos, NM 87545

(Dated: October 31, 2018)

Abstract

An implicit assumption made in the vast majority of studies of runaway electrons is that they are well confined to a given magnetic flux surface, thus allowing the use of slab or bounce averaged formulations that ignore the spatial transport of runaway electrons. While such an assumption is known to break down in the presence of strong 3D magnetic field perturbations, here we show that it can be violated even for an axisymmetric magnetic field under conditions representative of an actively mitigated disrupting plasma. Specifically, the low temperature and large impurity content typical of a post thermal quench plasma are shown to provide a drastic enhancement of the diffusive and convective transport of runaways electrons, where the convective component is found to be dominated by the Ware pinch. This inward convective flux allows runaway electrons to be displaced toward the plasma center, where they are eventually detrapped and reaccelerated, thus focusing populations of runaway electrons in the inner portion of the plasma. The resulting runaway electron distribution is shown to settle into a well-defined spatial eigenmode, whose form is often insensitive to the spatial distribution of the original seed population. The underlying transport processes responsible for determining the width and shape of the spatial runaway electron eigenmode are analyzed under a range of circumstances characteristic of a post thermal quench plasma.

I. INTRODUCTION

The formation of a large population of relativistic electrons during a tokamak disruption poses a significant risk to the success of large tokamaks such as ITER. A large effort has thus been focused on identifying means through which the formation of a large runaway electron population can be avoided, or if avoidance is not possible, means through which the most deleterious effects of runaway electrons can be mitigated. Under the assumption that runaway electrons are well confined to a given magnetic flux surface, a fairly clear theoretical picture has recently emerged with regard to the momentum space evolution of runaway electrons [1, 2], and consequently criteria through which they may be avoided [3, 4], or their energy controlled via self-generated micro-instabilities [5, 6] or externally injected waves [7]. One of the principal remaining uncertainties is with regard to the role that the transport of runaway electrons may play in modifying such avoidance criteria, or mitigation strategies.

At present, the majority of transport studies of runaway electrons have focused on the role of 3-D magnetic fields, and the subsequent rapid loss of runaway electrons along open magnetic field lines [8–11]. Little focus has been placed on transport in axisymmetric configurations. This emphasis is understandable given that runaway electrons are nearly collisionless, such that their collisional transport in a fully ionized low-Z plasma is exceptionally weak (see Sec. III below). In addition, magnetic surfaces are thought to be broken during the thermal quench phase of a disruption, allowing for the rapid loss of a significant fraction of any existing runaway electrons via parallel streaming [9–11]. This simple picture may, however, require amendment. In particular, after the thermal quench phase of a disruption, MHD modeling suggests that the magnetic flux surfaces tend to reform [12]. Under such circumstances losses of runaway electron via parallel streaming along open magnetic field lines will no longer be present. In contrast, as discussed in detail in Sec. III, the presence of large amounts of impurities in a low temperature plasma can significantly enhance the spatial transport of runaway electrons. Since several disruption mitigation schemes call for the injection of large amounts of impurities [13], this scenario is of particular importance for the description of runaway formation and evolution.

The enhancement of spatial transport by plasma impurities is due to two separate mechanisms. The first results from the dramatic enhancement of the pitch-angle scattering rate of runaway electrons in the presence of a background of partially ionized impurities [14, 15]. This in turn leads to a significant enhancement of the collisional diffusivity of runaway electrons. The second,

somewhat more subtle modification, follows from more detailed considerations of the phase space evolution of runaway electrons. Specifically, the enhanced pitch-angle scattering present in the system results in the runaway electron population having a broader distribution in pitch angle. As a result, a much larger trapped population of energetic electrons will be present compared to the case of a fully ionized low-Z plasma. Further noting that the enhancement of the collisional coefficients by the partially ionized impurities dramatically raises the threshold for the sustainment of the runaway electron population [16], a much larger inductive electric field is also necessarily present in order to sustain the runaway electron population. The combination of a significant energetic trapped particle fraction and a strong inductive electric field will result in a strong inward convection of the runaway population due to the Ware pinch [17, 18].

The presence of significant spatial transport, along with toroidal effects, leads to the formation of a non-trivial spatial profile of the runaway electron population. Specifically, as discussed further in Sec. IV, the strong inward convection of energetic trapped electrons facilitates the focusing of the runaway electron population to small radii. After a transient period, the resulting runaway electron population is shown to settle into a well defined eigenmode, in both momentum space [19] and configuration space. An important feature of the dynamics of the system is that the presence of significant spatial transport allows the system to access the global eigenmode (nearly) irrespective of the spatial distribution of the 'seed' electron population. This behavior cannot be captured by 0D-2V formulations which have to date provided the foundations for our understanding of runaway dynamics. A principal thrust of this work will be to identify circumstances under which, even in an axisymmetric plasma, 0D-2V formulations will be insufficient for describing the formation and evolution of a runaway population.

The remainder of this paper is organized as follows. Section II describes the model equations that are evolved along with a discussion of key idealizations made in the subsequent sections. The transport of runaway electrons in a fully ionized low-Z plasma is contrasted with the disruption relevant scenario of a plasma containing a large fraction of partially ionized impurities in Sec. III. Section IV describes the phase space evolution of a runaway electron population in the presence of partially ionized impurities. Conclusions and a brief discussion are given in Sec. V.

II. MODEL EQUATIONS

This section gives a brief overview of the system of equations solved along with the key idealizations invoked throughout the following sections. A more detailed discussion is provided in Ref. [20]. A particle based approach is used throughout this work, where the electron orbits are evolved using a 5-D system of guiding-center equations. Small-angle collisions are described via a Monte-Carlo collision operator [21], and synchrotron radiation is also retained. Large-angle collisions are described by a secondary source term [22–25] that accounts for the momentum space distribution of runaway electrons providing a means of accurately describing the avalanche of runaway electrons.

Three key idealizations will be invoked in the following analysis. These can be enumerated as:

1. a spatially and temporally constant loop voltage is assumed,

2. the dimensionless parameter $(c\tau_c/a)$, which is proportional to the ratio of the collisional to transit time scales, is taken to be fixed throughout several parameter scans. Here $\tau_c \equiv 4\pi\epsilon_0^2 m_e^2 c^3/n_e e^4 \ln\Lambda_0$ is related to the collision time of a relativistic electron, n_e is the free electron density, $\ln\Lambda_0$ is the Coulomb logarithm of a thermal electron, a is the minor radius, m_e the electron rest mass, c is the speed of light, e the electron charge, and ϵ_0 is the permittivity of free space.

3. an absorbing boundary condition is assumed at low energy and at a radius of $r/a = 1$.

Item 1. is a valid idealization in the limit where runaway electrons carry a negligible fraction of the plasma current. In the opposite limit, where the runaway electrons carry the majority of the plasma current, feedback of the runaway electrons onto Ohm's law cannot be neglected, such that the inductive electric field and runaway electron population will have to be evolved self-consistently (see Ref. [26], for example). Such a thrust will be pursued in a future work. With regard to item 2., the parameter $(c\tau_c/a)$ scales inversely with machine size and the free electron density n_e, and thus will have a broad range of values $(10^5 - 10^8)$ depending on the specific characteristics of the discharge and the device considered. Since the motivation of the present work is not to model a specific discharge, this parameter will generally be taken to have a constant value (typically, $c\tau_c/a = 5 \times 10^5$) during the parameter scans carried out in Sec. IV below. Our motivation for choosing a relatively small value of $(c\tau_c/a)$ is that the numerical cost of the simulations scales approximately linearly with $(c\tau_c/a)$. Specifically, the phase space dynamics of

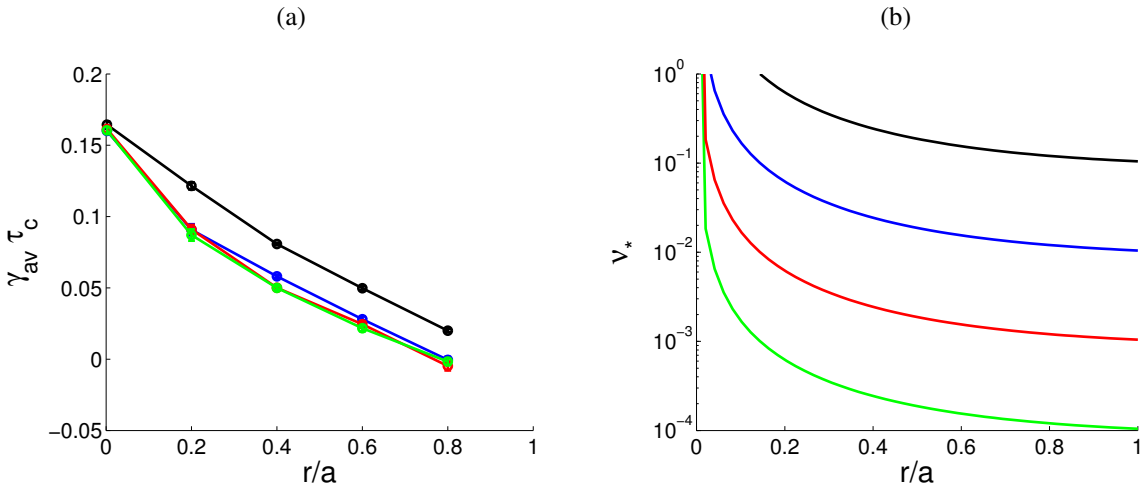

Figure 1. (a) Avalanche growth rate as a function of radius for different values of $(c\tau_c/a)$. The black curve is for $(c\tau_c/a) = 5\times10^3$, the blue curve is for $(c\tau_c/a) = 5\times10^4$, the red curve is for $(c\tau_c/a) = 5\times10^5$, and the green curve is for $(c\tau_c/a) = 5\times10^6$. (b) Values of $\nu_* \equiv \varepsilon^{-3/2}\nu_D^{ps}\,(qR_0/v)$ as a function of radius for different values of $(c\tau_c/a)$, where ν_D^{ps} is the pitch-angle scattering frequency defined by Eq. (5). The energy at which ν_* is evaluated is chosen to be $\gamma = 3.53$, which is the approximate location of the X-point [2] of the runaway electron primary distribution. This value generally sets the minimum energy a secondary electron requires in order to run away [20]. The color scheme is the same as (a). The other parameters were taken to be $n_{Ar}^+ = n_D$, $a/R_0 = 1/3$, $\bar{E}_1 = 19.5$, $\bar{\alpha} \equiv \tau_c/\tau_s = 0.05$, τ_s is the time scale for synchrotron radiation losses, $T_e = 2$ eV, $\ln\Lambda_0 = 10$, $q_0 = 2.1$, $q_2 = 2$, and we considered a large tokamak ($a = 200$ cm) with an exceptionally large magnetic field ($B_0 = 53$ T) such that radial transport can be neglected.

the runaway electrons takes place on a time scale of several τ_c, whereas the parameter $(c\tau_c/a)$ is proportional to the number of electron transits that are executed during each τ_c. Thus, as $(c\tau_c/a)$ is increased the normalized time step $\Delta t/\tau_c$ employed when evolving the guiding-center motion must be correspondingly reduced.

It may be readily verified that for sufficiently large $(c\tau_c/a)$, the phase space dynamics of the runaway electrons (avalanche growth rate, threshold, and collisional transport) are invariant as $(c\tau_c/a)$ is varied (with appropriate normalizations). Two example cases are shown in Figs. 1 and 2. Figure 1(a) shows the avalanche growth rate for different values of $(c\tau_c/a)$. As discussed further in Sec. III A, the exceptionally large magnetic field used in this example case will result in a negligible amount of spatial transport for this axisymmetric case, such that the avalanche growth rate can be computed on a flux surface by flux surface basis. Here it is evident that for

sufficiently large $(c\tau_c/a)$ the avalanche growth rate normalized to τ_c becomes insensitive to the specific value of $(c\tau_c/a)$. The underlying physics behind this asymptotic scaling is that for $\nu_* \equiv \varepsilon^{-3/2}\nu_D^{ps}\left(qR_0/v\right) \gtrsim 1$ [$\varepsilon \equiv r/R_0$, r is the radial coordinate, v is the speed coordinate, R_0 is the major radius at the magnetic origin, the safety factor is defined by $q \equiv rB_0/R_0B_\theta\left(r\right)$, and the safety factor is assumed to have the form $q\left(r\right) = q_0 + q_2r^2$], the collisional detrapping rate is faster than the bounce time of the electron (ν_D^{ps} is the pitch-angle scattering frequency defined by Eq. (5) below). Since a principal impact of toroidicity on the avalanche growth rate results from the trapping of secondary electrons by the inhomogeneous tokamak magnetic field, this trapping effect will be underestimated for $\nu_* \sim \mathcal{O}\left(1\right)$. This leads to a higher predicted avalanche growth rate for cases with smaller $(c\tau_c/a)$ at all radial locations [see Figs. 1(a) and 1(b)], except at $r/a \approx 0$ where the trapped region occupies a small fraction of momentum space. In contrast, once $\nu_* \ll 1$ secondary electrons born in the trapped region will be reflected several times before being detrapped (i.e. the system is in the banana regime). These trapped electrons will thus not be accelerated by the electric field, and will thus be lost to the bulk plasma. This tends to reduce the avalanche growth rate compared to the $\nu_* \sim \mathcal{O}\left(1\right)$ cases. Once ν_* becomes asymptotically small, however, the growth rate of the system asymptotes to a constant value (when normalized to τ_c), as anticipated for systems that are asymptotically in the banana regime.

A second, more stringent comparison, is shown in Fig. 2. Here, the spatial evolution of the flux surface averaged runaway electron population is plotted for different values of $(c\tau_c/a)$. While the specific physics underlying this spatial evolution will be the subject of Secs. III and IV, it is again apparent that the spatial-temporal evolution of runaway electrons is invariant for the two values of $(c\tau_c/a)$ considered in these simulations. Physically, this is again due to the system being in the banana regime, such that collisional transport physics does not change as $(c\tau_c/a)$ is scanned. Two caveats to this behavior should be mentioned. The first is that although the evolution of the system when normalized to τ_c is invariant for sufficiently large $(c\tau_c/a)$, the physical time that transpires scales linearly with $(c\tau_c/a)$ (for the same minor radius a). Thus, in dimensional units the amount of time that transpired in the two cases shown in Fig. 2 would deviate by an order of magnitude. In addition, this insensitivity to $(c\tau_c/a)$ is only valid for closed field lines. Specifically, in the limit of low collisionality, the diffusion of a relativistic test particle in a stochastic magnetic field is predicted to scale as $\tau_c D_{st}/a^2 \propto \left(qR_0/a\right)\left(c\tau_c/a\right)\left(\delta B/B_0\right)^2$ [27] (neglecting orbit width effects). Here, δB is the magnitude of the perturbed magnetic field. For such cases the relative importance of collisional transport and losses through parallel streaming will scale with $(c\tau_c/a)$.

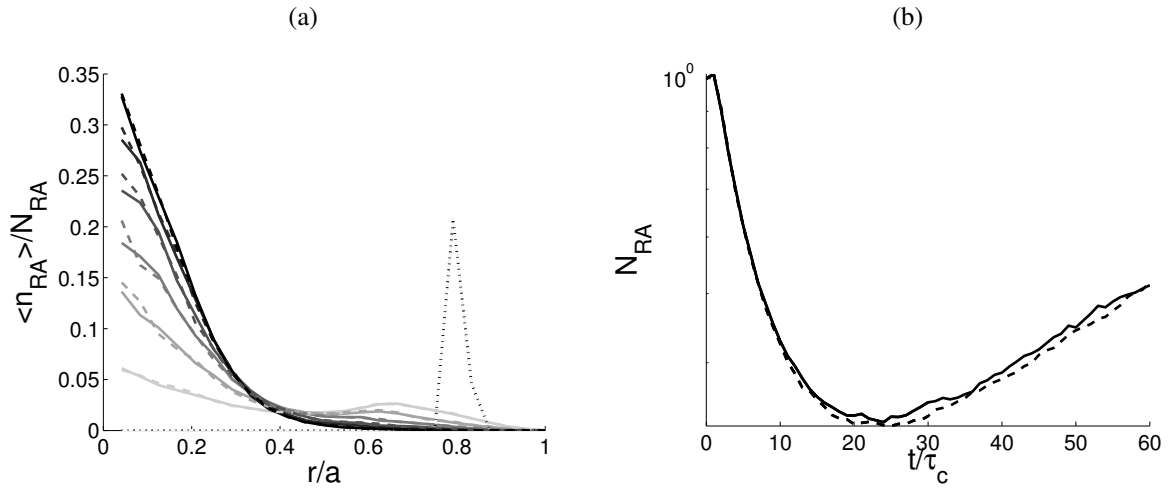

Figure 2. (a) Flux surface averaged density of runaway electrons normalized to the total number of runaway electrons N_{RA}. The solid curves indicates a case with $c\tau_c/a = 5 \times 10^5$ whereas the dashed curves indicate a case with $c\tau_c/a = 5 \times 10^6$. Light colors indicate early times and become progressively darker as time evolves (intervals of $5\tau_c$). The dotted curve indicates the initial condition. (b) Total number of runaway electrons versus time. Solid and dashed curves for $c\tau_c/a = 5 \times 10^5$ and $c\tau_c/a = 5 \times 10^6$, respectively. The parameters were taken to be $E/E_c = 17$, $\bar{\alpha} = 0.05$, $T_e = 2$ eV, $\ln \Lambda_0 = 10$, $q_0 = 2.1$, $q_2 = 2$, $a = 60$ cm, $B_0 = 1.5$ T. The argon was assumed to be singly ionized with $n_{Ar}^+ = n_D$.

The third idealization employed in this work will be the enforcement of absorbing boundary conditions at low energy and $r/a = 1$. The absorbing boundary condition at $r/a = 1$ is intended to mimic the loss of electrons to the wall, albeit in an idealized way. A somewhat more impactful idealization is the absorbing boundary condition at low energy. While in a confined keV plasma such an absorbing boundary condition would neglect the significant Dreicer flux of electrons being accelerated from the bulk to high energy, for the low temperature plasmas considered below (T_e of a few to several eV) such a local acceleration process will have a negligible effect on the runaway evolution. Thus, the principal impact of this idealization is that we will not be able to model the initial 'seed' formation of runaway electrons, but will instead assume an initial population of runaway electrons is present in order to initiate the avalanche instability.

III. TRANSPORT OF RUNAWAY ELECTRONS IN AXISYMMETRIC GEOMETRY

This section will be concerned with contrasting the collisional transport of runaway electrons in a fully ionized low-Z plasma with the disruption relevant case of a plasma containing a significant

population of partially ionized impurities. We will begin by providing scaling estimates of the collisional transport of runaway electrons in a low-Z fully ionized plasma. These estimates will then be verified by Monte Carlo transport simulations. Subsequently, the role of partially ionized impurities in enhancing this transport is discussed in Sec. III B. For all the results described in this section, the large-angle collision operator will be turned off such that the computed transport will be due to the primary electron population.

A. Fully Ionized Low-Z Plasma

The level of collisional transport present in a fully ionized low-Z plasma can be straightforwardly estimated for both thermal and runaway electrons. Specifically, since the banana orbit width for non-relativistic electrons scales as $\Delta r \sim v/\omega_{c\theta}$ ($\omega_{c\theta}$ is the electron cyclotron frequency using the poloidal magnetic field), and noting $\nu_D \sim (Z_{eff}+1)/v^3$ for non-relativistic electrons, the resulting diffusivity can be estimated as:

$$\frac{\tau_c D_{non-rel}}{a^2} = A f_t \frac{\Delta r^2}{2a^2}\tau_c \nu_D = A\frac{f_t}{2}\left(\frac{c}{a\omega_{c\theta}}\right)^2 \frac{c}{v}\left(Z_{eff}+1\right), \tag{1}$$

where A is an order one numerical value, f_t is the trapped particle fraction, and Z_{eff} is the effective charge. This estimate is only valid in the low collisionality limit, where $\nu_* \ll 1$. For the specific case of a Lorentz collision operator, the precise analytic form in the small inverse aspect ratio limit can be recovered by taking $A f_t \approx 0.689\sqrt{2\varepsilon}$ [21, 28] (assuming $v \gg v_{Te}$, such that the Chandrasekhar functions take a simple form). For relativistic electrons, the pitch-angle scattering frequency and banana width instead scale as $\nu_D \sim (Z_{eff}+1)/p^2$ and $\Delta r \sim c\gamma/\omega_{c\theta}$, such that

$$\frac{\tau_c D_{rel}}{a^2} \approx f_t^{RA}\frac{\Delta r^2}{2a^2}\tau_c\nu_D \approx \frac{f_t^{RA}}{2}\frac{c^2\gamma^2}{a^2\omega_{c\theta}^2}\frac{Z_{eff}+1}{p^2} \approx \frac{f_t^{RA}}{2}\left(\frac{c}{a\omega_{c\theta}}\right)^2\left(Z_{eff}+1\right). \tag{2}$$

Here f_t^{RA} is the trapped particle fraction for runaway electrons, $p \equiv \gamma m_e v$ is the momentum, and $\gamma \equiv 1/\sqrt{1-v^2/c^2}$ is the Lorentz factor. The neoclassical diffusivity of the runaway electrons is thus anticipated to be reduced compared to thermal electrons by a factor of order $D_{rel}/D_{non-rel} \sim \left(f_t^{RA}/f_t\right)(v_{Te}/c) \ll 1$, where v_{Te} is the thermal electron velocity. Based on this simple estimate, the collisional transport of runaway electrons is expected to be diminished compared to that of thermal particles due to (i) the weaker pitch-angle scattering of runaway electrons compared to thermal electrons, (ii) and the often negligibly small number of trapped runaway electrons.

As a means of obtaining transparent estimates of the magnitude of runaway electron transport in a small inverse aspect ratio axisymmetric equilibrium it will be useful to define reference values

of the collisional diffusivity and convection velocity. For a fully ionized plasma, a reference collisional diffusivity can be defined as

$$\frac{\tau_c^a D_0}{a^2} \equiv 0.689\sqrt{2\varepsilon}\left(\frac{c}{a\omega_{c\theta}}\right)^2\frac{(Z+1)}{2} \approx 0.689\sqrt{2\varepsilon}\left(\frac{c}{a\omega_{ce}}\right)^2\left(\frac{qR_0}{r}\right)^2\frac{(Z+1)}{2}, \tag{3}$$

where Z is the charge state of the main ion species (hydrogen or helium for the example cases given below), τ_c^a is defined analogously to τ_c, but using the free electrons associated with the main ion species, rather than the total density of free electrons. For a pure plasma $\tau_c^a = \tau_c$, but for the case where impurities are present $\tau_c^a > \tau_c$, since the free electrons associated with the impurity population will reduce the relativistic collision time. In addition, it will also be useful to define the reference convection velocity by

$$\frac{\tau_c^a V_0}{a} \equiv \left(\frac{c}{\omega_{ce}a}\right)\left|\left(\frac{\mathbf{E}}{E_c}\times\hat{\mathbf{b}}\right)\cdot\hat{\mathbf{r}}\right| \approx \left(\frac{c}{a\omega_{ce}}\right)\frac{r}{qR_0}, \tag{4}$$

which corresponds to the inward $\mathbf{E}\times\mathbf{B}$ flow for an inductive electric field at the Connor-Hastie threshold in a pure plasma. From these reference transport coefficients, it may be straightforwardly verified that for large devices such as ITER, runaway electron transport will be negligible for an axisymmetric fully ionized low-Z plasma. Specifically, at mid radius $r/a = 0.5$, for ITER like parameters ($n_e = 10^{14}$ cm^{-3}, $B_0 = 5.3$ T, $\ln\Lambda_0 = 15$, $a = 200$ cm, $q = 2$, $a/R_0 = 1/3$) $\tau_c^a D_0/a^2 \approx 1.5\times10^{-6}$ and $\tau_c^a V_0/a \approx 1.3\times10^{-5}$, where $\tau_c^a \approx 22$ ms. An effective confinement time for runaway electrons can then be estimated as $\tau_{conf}/\tau_c^a = a^2/\left(\tau_c^a D_0\right) \approx 7\times10^5$, or around 4 hours. For a mid size tokamak such as DIII-D (same parameters as above but now with $B = 1.5$ T and $a = 60$ cm) $\tau_c^a D_0/a^2 \approx 2.1\times10^{-4}$ and $\tau_c^a V_0/a \approx 1.6\times10^{-4}$, implying an effective confinement time of $\tau_{conf}/\tau_c^a = a^2/\left(\tau_c^a D_0\right) \approx 5\times10^3$, or around 107 seconds. In either case, transport in an axisymmetric hydrogen plasma is unlikely to qualitatively modify results from calculations assuming the runaway electrons to be localized about a given flux surface.

In order to verify these trends, the Monte Carlo solver described in Sec. II will be used. Employing the procedure outlined in Appendix A for extracting the particle diffusivity, the computed diffusivity for electrons with different energies is shown in Fig. 3. Here, we have turned off the inductive electric field, synchrotron radiation and collisional drag terms. We have, however, retained the pitch-angle scattering term such that a base level of neoclassical transport is present. In addition, under these assumptions the electrons will be isotropically distributed in pitch-angle. As the energy of the electron population is increased the diffusivity reduces until it reaches an asymptotic value of $D/D_0 \sim 1.0$ for electrons with energies in the MeV range. We note in passing that for

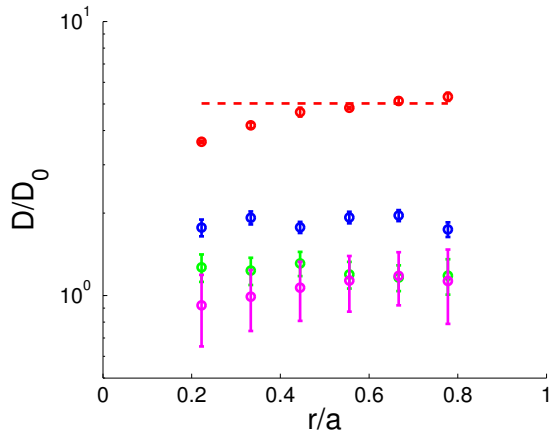

Figure 3. Computed diffusivity normalized to the reference diffusivity defined by Eq. (3). The red markers are for an electron population with 10 keV, the blue markers is for 100 keV, the green markers are for 500 keV, and the magenta markers are for 1.5 MeV. The red dashed curve is the scaling estimate given by Eq. (1). The other parameters were taken to be $a/R_0 = 1/3$, $(c\tau_c/a) = 5 \times 10^6$, $Z = 2$, $\bar{E}_1 = 0$, $\bar{\alpha} = 0$, $v_{Te}/c = 0.0063$, $q_0 = 2.1$, $q_2 = 2$ and we considered an ITER like case ($a = 200$ cm, $B_0 = 5.3$ T). The drag term was also turned off in this simulation. The integrations were performed for 20 collision times. The normalizing factor D_0 is defined in Eq. (3).

the non-relativistic case the computed value of the diffusivity deviates from the theoretical value at small radii. This is due to $\nu_* \propto \varepsilon^{-3/2}$, such that this value increases near the origin. In particular, for the case of a 10 keV electron, $\nu_* \approx 0.13$ at a radius of $r/a \approx 0.2$ for the parameters employed here. This value of ν_* is too large for the system to asymptote to a banana regime scaling, which is the limit assumed in the derivation of Eq. (1). It has been verified that for sufficiently large $c\tau_c/a$ (small ν_*), the diffusivity for thermal electrons is accurately computed by the Monte Carlo solver at small radii.

The estimate of the diffusivity shown in Fig. 3 corresponds to a significant overestimate of the collisional transport anticipated from a runaway electron population. This follows, since the inductive electric field was neglected in that example case, resulting in an isotropic electron distribution. The incorporation of an inductive electric field above the Connor-Hastie threshold [29] will result in a highly anisotropic electron distribution function at high energies (see Fig. 4), with the majority of runaway electrons localized to the $\xi = -1$ axis. Since the level of collisional transport depends sensitively on the trapped particle fraction, the transport from a population of runaway electrons including the inductive electric field (along with frictional drag and radiation)

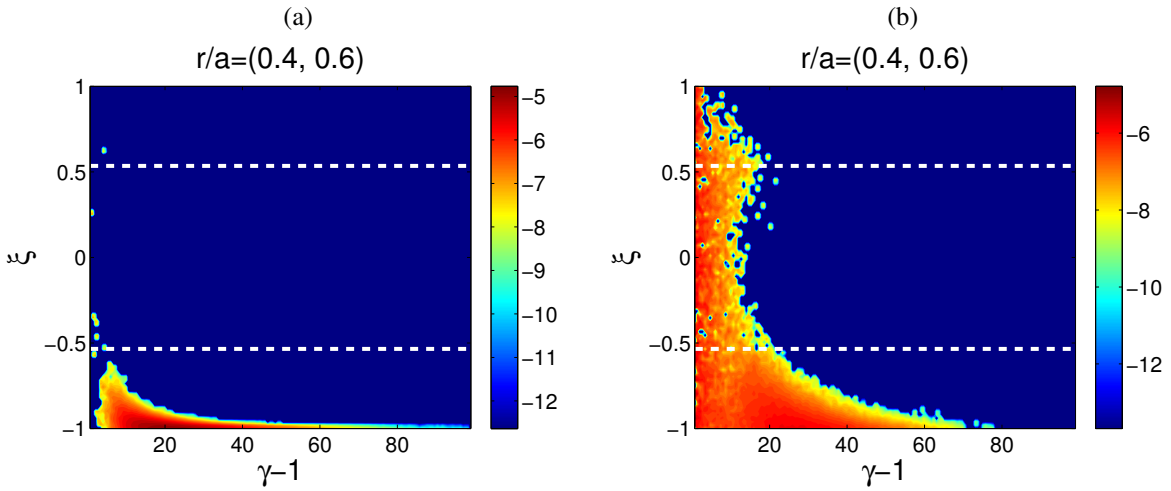

Figure 4. Momentum space distribution of electrons between $r/a = (0.4, 0.6)$ and $\theta = (-\pi/10, \pi/10)$ for a pure hydrogen plasma (a) and a plasma containing singly ionized argon with $n^+_{Ar} = n_D$ (b). The horizontal dashed white lines indicate the trapped-passing boundary at $r/a = 0.5$. The electric field in both cases was chosen to be somewhat above marginality with $\bar{E}_1 = 2$ for the left panel and $\bar{E}_1 = 19.49$ in the right panel. The other parameters are were taken to be $a/R_0 = 1/3$, $(c\tau_c/a) = 5 \times 10^5$, $\bar{\alpha} = 0.05$, $T_e = 10$ eV, $q_0 = 2.1$, $q_2 = 2$ and we considered an ITER like case ($a = 200$ cm, $B_0 = 5.3$ T).

can be anticipated to be far weaker than for the case considered in Fig. 3. This is made evident in Fig. 5, where the transport level computed for a primary runaway distribution function is several orders of magnitude below the reference diffusivity of relativistic electrons defined by Eq. (3). We also note that the presence of a toroidal inductive electric field results in an inward drift, as made evident in Fig. 5(a). This inward drift motion results from both the $\mathbf{E} \times \mathbf{B}/B^2 \propto E_\varphi B_\theta / B^2$, drift along with the Ware pinch, whose velocity scales as $V_{Ware} \propto -(E_\varphi / B_\theta)$. While the velocity associated with the Ware pinch has a much larger magnitude than the $\mathbf{E} \times \mathbf{B}$ drift (approximately two orders of magnitude at mid radius for this case), the Ware pinch only affects trapped particles. As a result, it only has a modest influence on the computed convection velocity in this case, which is for a low-Z fusion plasma of hydrogen isotopes and helium. We note that the horizontal (major radius) drifts of passing runaway electrons described in Refs. [30, 31] do not factor into the above analysis. This follows since a net drift resulting from this mechanism requires the acceleration or deceleration of an electron population. The above estimate of the transport coefficients, however, was based on an approximately steady state runaway distribution.

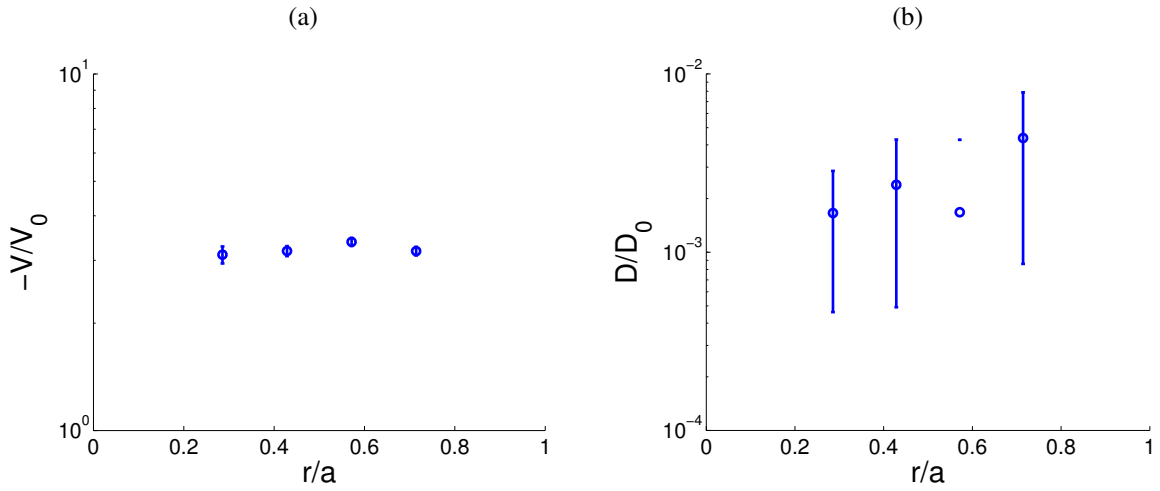

Figure 5. Estimated convective transport coefficient (a) and diffusivity (b) for different radii. The parameters are the same as those used in Fig. 4(a), except with $\bar{E}_1 = 1.75$. The normalizing factors D_0 and V_0 are defined in Eqs. (3) and (4).

B. Partially Ionized Plasma

The presence of partially ionized impurities can strongly impact the collisionality of runaway electrons, and thus potentially their spatial transport. In particular, a simple form for the pitch-angle scattering coefficient in the presence of a population of ions in a general charge state can be written as [15]

$$\tau_c \nu_D^{ps} \approx \frac{\gamma}{p^3}\left\{ Z_{eff}\frac{\ln\Lambda_{ei}}{\ln\Lambda_0} + \frac{1}{\ln\Lambda_0}\sum_j \frac{n_j}{n_e} g_j\left(p\right) + \frac{\ln\Lambda_{ee}}{\ln\Lambda_0}\right\}, \tag{5}$$

where

$$g_j\left(p\right) \approx \left(Z_{0,j}^2 - Z_j^2\right)\ln\left(\frac{2a_j}{\alpha}p\right) - \frac{2}{3}\left(Z_{0,j} - Z_j\right)^2. \tag{6}$$

Here, $Z_{0,j}$ is the atomic number of the ion, Z_j is the charge state, n_j is the density of ions in a given charge state, $\alpha \approx 1/137$ is the fine structure constant, $\ln\Lambda_0$ is the Coulomb logarithm for thermal electrons, a_j is the effective ion size in units of the Bohr radius, and $\ln\Lambda_{ei}$ and $\ln\Lambda_{ee}$ are the electron-ion and electron-electron Coulomb logarithms for relativistic electrons, respectively. These Coulomb logarithms generally depend on energy, with their explicit form given in Ref. [15]. The first term in Eq. (5) describes electron-ion scattering by the completely screened ion, the second term describes the impact of partial screening, and the third term describes electron-electron scattering. For a case of a mid to high Z ion in a low charge state ($Z_{0,j}^2 \gg Z_j^2$), and noting that typically $2a_j p/\alpha \gg 1$ for relativistic electrons [15], $g_j\left(p\right) \gg 1$ such that partial screening

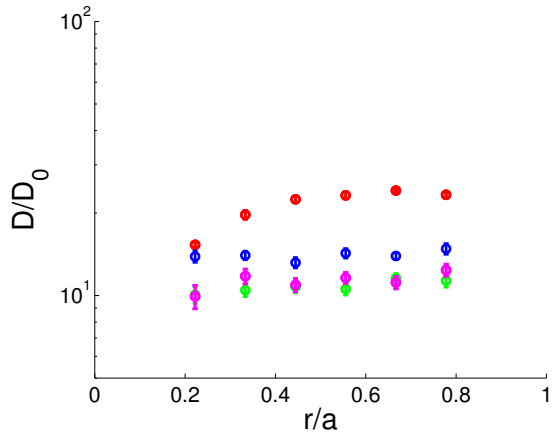

Figure 6. Computed diffusivity normalized to the reference diffusivity defined by Eq. (3) for a system composed of deuterium and singly ionized argon with $n^+_{Ar} = n_D/10$. The red markers are for an electron population with 10 keV, the blue markers are for 100 keV, the green markers are for 500 keV, and the magenta markers are for 1.5 MeV. The other parameters were taken to be $a/R_0 = 1/3$, $(c\tau_c/a) = 5 \times 10^6$, $\bar{E}_1 = 0$, $\bar{\alpha} = 0$, $v_{Te}/c = 0.0063$, $q_0 = 2.1$, $q_2 = 2$ and we considered an ITER like case ($a = 200$ cm, $B_0 = 5.3$ T). The integrations were performed for 20 collision times. The collisional drag was also turned off in this simulation. The normalizing factor D_0 is defined in Eq. (3).

will drastically enhance the pitch-angle scattering rate compared to the completely screened limit. The collisional diffusivity for relativistic electrons evolving in the presence of partially ionized impurities then becomes

$$\frac{\tau_c D^{ps}_{rel}}{a^2} \approx f_t^{RA} \frac{\Delta r^2}{2a^2} \tau_c \nu_D^{ps} \approx \frac{f_t^{RA}}{2} \frac{c^2\gamma^2}{a^2\omega_{c\theta}^2} \frac{1}{p^2} \tau_c C_B \approx \frac{f_t^{RA}}{2} \left(\frac{c}{a\omega_{c\theta}} \right)^2 \tau_c C_B, \tag{7}$$

where

$$\tau_c C_B \equiv p^2 \left(\tau_c \nu_D^{ps} \right). \tag{8}$$

In contrast to the case of a fully ionized plasma, the diffusivity given by Eq. (7) does not asymptote to a constant value at high energy. Instead, the quantity C_B will continue to increase with the energy of the electron. The energy dependence of C_B is, however, only logarithmic [primarily arising from $g_j(p)$]. A verification of this scaling for conditions similar to those used in Fig. 3, but with singly ionized argon added with a density $n^+_{Ar} = n_D/10$ is shown in Fig. 6. Here it is apparent that the presence of a moderate amount of argon increases the level of transport modestly for keV electrons, and much more significantly for MeV electrons compared to a fully ionized low-Z plasma. Furthermore, the reduction of the diffusivity between 10 keV and 1.5 MeV electrons is

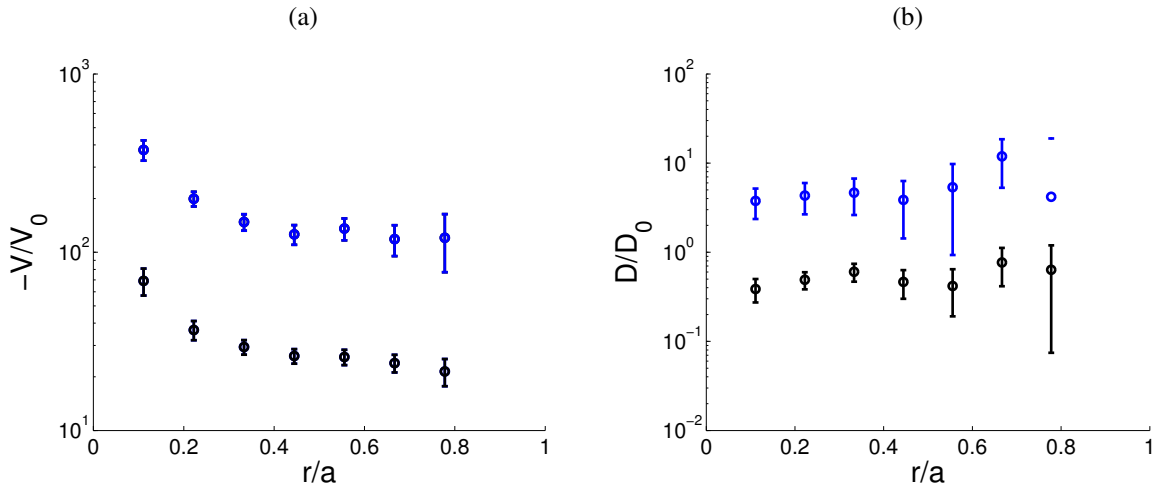

Figure 7. Computed convective transport coefficient (a) and diffusivity (b) for different radii and different amounts of argon impurities. The black markers are for $n^+_{Ar} = n_D/10$ whereas the blue markers are for $n^+_{Ar} = n_D$. In both cases the inductive electric field chosen was such that the system was just above marginality ($\bar{E} = 6.27$ for $n^+_{Ar} = n_D/10$, and $\bar{E} = 19.49$ for $n^+_{Ar} = n_D$). The other parameters were taken to be $a/R_0 = 1/3$, $(c\tau_c/a) = 5 \times 10^5$, $\bar{\alpha} = 0.05$, $v_{Te}/c = 0.0063$, $q_0 = 2.1$, $q_2 = 2$ and we considered a large tokamak ($a = 200$ cm) with a very strong magnetic field ($B_0 = 53$ T) in order to allow an accurate evaluation of the transport coefficients at a given radius when large amounts of argon are present. The particles were initialized with $r/a = (0, 0.8)$. The normalizing factors D_0 and V_0 are defined in Eqs. (3) and (4).

significantly less than the fully ionized case. Moreover, due to C_B increasing logarithmically with energy, this difference would continue to narrow for higher energy electrons.

Analogous to the case of a fully ionized low-Z plasma discussed in Sec. III A, the transport computed from a runaway electron distribution will generally be much less than for the case of the isotropic distribution assumed in Fig. 6. The computed collisional diffusivity for different amounts of argon impurities is shown in Fig. 7(b). Here, it is apparent that while the collisional diffusivity is greatly reduced compared to the case of an isotropic plasma, it still far exceeds that of a fully ionized low-Z plasma. In addition, the diffusivity scales approximately linearly with the amount of argon in the plasma, such that this level of transport can be further enhanced by increased argon injection.

The underlying inward convection velocity of runaway electrons is also significantly enhanced for the case of a significant impurity population. This follows due to both the larger inductive electric field necessary to sustain a population of runaway electrons, and the increase in the number

of trapped energetic electrons [see Fig. 4(b)]. Such energetic electrons are convected inward rapidly by the Ware pinch, which generally exceeds the inward $\mathbf{E} \times \mathbf{B}$ flow by roughly two orders of magnitude. This is made evident in Fig. 7(a), where the convective velocity can be enhanced by more than two orders of magnitude for $n_{Ar}^{+} = n_D$, and will continue to increase as the amount of argon is increased. We note that while the value of the normalized inward convection velocity increases in Fig. 7 for small radii, this is due to the normalization V_0 scaling with the minor radius and thus diverging at small radius.

IV. SPATIAL EVOLUTION OF A RUNAWAY POPULATION

From the discussion in Sec. III it is apparent that impurities can significantly enhance both the diffusive and convective transport of runaway electrons. The increase of the diffusivity above the reference value D_0 is generally modest for the cases considered, whereas the inward convective velocity can be increased drastically (see Fig. 7). This observation suggests that while collisional transport generally will not increase the radial loss of runaway electrons (since $\tau_c D/a^2 \approx \tau_c^a D_0/a^2 \ll 1$), the presence of a drastically enhanced inward convection velocity will provide a means of modifying the runaway electrons' spatial profile. In this section we will be interested in identifying circumstances where the transport of runaway electrons is sufficiently strong such that the commonly employed idealization of solving for the runaway electron population one flux surface at a time will break down. As will be made evident below, the inclusion of large-angle collisions will be essential for obtaining an accurate spatial profile of runaway electrons. Thus, avalanche physics will also be incorporated for the studies carried out in this section. For all of the cases considered below, the loop voltage will be taken to be a constant such that these scenarios are only appropriate in the limit where the runaway electron population is sufficiently small such that they carry a negligible fraction of the plasma current. In the opposite limit, the evolution of the inductive electric field will need to be evolved self-consistently. This latter limit will be the subject of future work.

A. Runaway Spatial Eigenmode

Considering a case of a plasma containing a significant impurity population, the spatial evolution of the runaway profile is shown in Fig 8(a). Here, the seed runaway electron population

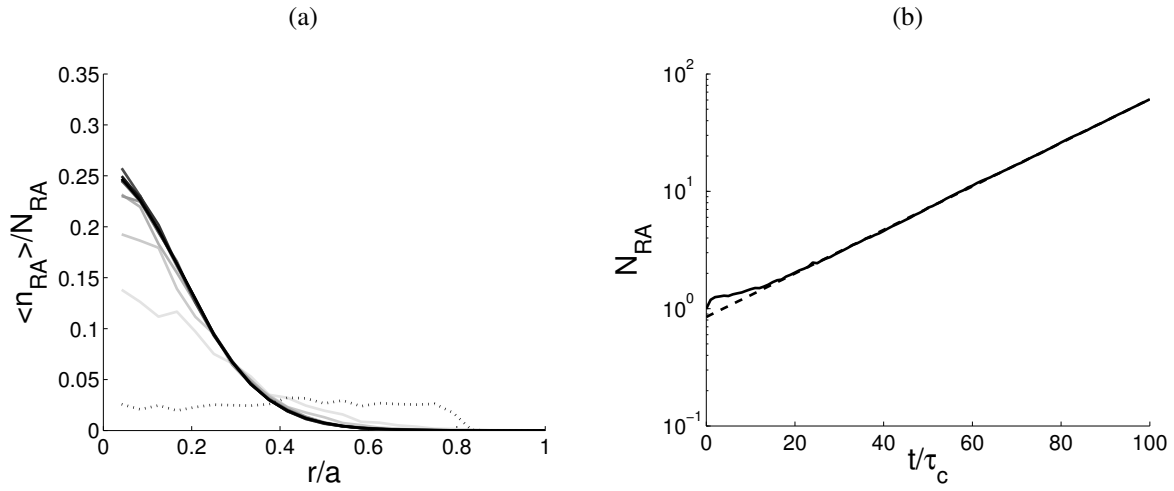

Figure 8. (a) Flux surface averaged density of runaway electrons normalized to the total number of runaway electrons. The dotted curve indicates the initial condition, whereas the solid curves indicate time slices (at intervals of 10 τ_c) of the flux surface averaged runaway distribution. Light colors indicate early times and become progressively darker as time evolves. (b) Number of runaway electrons as a function of time. The parameters were taken to be $E/E_c = 17.5$, $\bar{\alpha} = 0.05$, $T_e = 2$ eV, $\ln\Lambda_0 = 10$, $q_0 = 2.1$, $q_2 = 2$, $c\tau_c/a = 5 \times 10^5$, $a = 60$ cm, $B_0 = 1$ T. The argon was assumed to be singly ionized with $n_{Ar}^+ = n_D$.

is assumed to be distributed uniformly in space between $r/a = (0, 0.8)$, localized to high energy $\gamma = (10, 20)$, and approximately directed along the equilibrium magnetic field $\xi = (-0.8, -1)$. The impurity ions are assumed to be composed of singly ionized argon with $n_{Ar}^+ = n_D$. For simplicity, we assume the density and temperature profiles to be constant in space and time. As evident from Fig. 8, the initially spatially homogeneous profile of runaway electrons evolves into a centrally peaked runaway electron distribution function. While the number of runaway electrons increases in time, the normalized spatial profile of runaway electrons asymptotes to a characteristic shape. Furthermore, after a transient period of approximately $20\tau_c$, the growth of the global runaway electron population obeys an exponential scaling [see Fig. 8(b)]. These two observations suggest that the runaway electron population evolves into a global eigenmode.

The formation of this runaway eigenmode results both from the avalanche growth rate generally being larger near the tokamak magnetic axis along with the spatial transport of runaway electrons as described in Sec. III. The first process is largely a result of particle trapping reducing the rate at which secondary electrons can run away. Since the trapped region increases with increasing radius, this effect becomes more prominent near the tokamak edge. As a consequence, for constant density profiles such as assumed here, runaway electrons will avalanche more rapidly in the tokamak core,

thus driving a centrally peaked runaway electron profile. This physics is independent of transport, and thus can be described by formulations evolving the runaway electron distribution on a flux surface by surface basis.

The second piece of critical physics is linked to the spatial transport of runaway electrons. Specifically, the finite width of the runaway eigenmode results either from the finite orbit width of the runaway electrons or the presence of a collisional diffusivity limiting the radial gradient of the runaway electron population. As discussed in Sec. IV B, the scaling of the eigenmode width with magnetic field strength B_0 is not consistent with the finite orbit width playing the dominant role for the parameter regime considered here. This suggests that collisional diffusion is responsible for setting the eigenmode width. A somewhat subtler transport effect is related to the role of the inward convection of runaway electrons highlighted in Sec. III. In order to understand this transport process in more detail, it will be useful to consider the evolution of a ring of runaway electrons initially localized at a radius of $r/a \approx 0.8$. Such a case is shown in Fig. 9. After a short transient the runaway electron distribution broadens significantly in pitch, allowing a significant number of energetic electrons to enter the trapped region. In the presence of the strong inductive electric field necessary to sustain the runaway electron population ($E/E_c \sim 17$, in this case), these trapped energetic electrons are rapidly convected inward by the Ware pinch. This is made evident by the spatial distribution of runaway electrons at $t/\tau_c = 0.5$. Here aside from the broadening of the initial ring of electrons, a non-negligible number of energetic electrons are evident at small radii. As these energetic trapped electrons propagate inward, the trapped region of momentum space contracts, allowing a fraction of the trapped electrons to be detrapped at smaller radii, and hence reaccelerated by the inductive electric field. Such electrons act as a seed population at small radii, which triggers an avalanche instability near the magnetic axis. As time evolves the runaway distribution settles into the eigenmode distribution described above. Thus, the presence of strong spatial transport allows the runaway electron population to settle into a well defined eigenmode nearly independent of the initial spatial distribution of the seed population.

B. Mode Width and Relaxation Time of Runaway Spatial Eigenmode

In order to provide a more detailed characterization of the formation of the spatial runaway eigenmode, we will seek to identify the quantities that set the saturated width and the relaxation

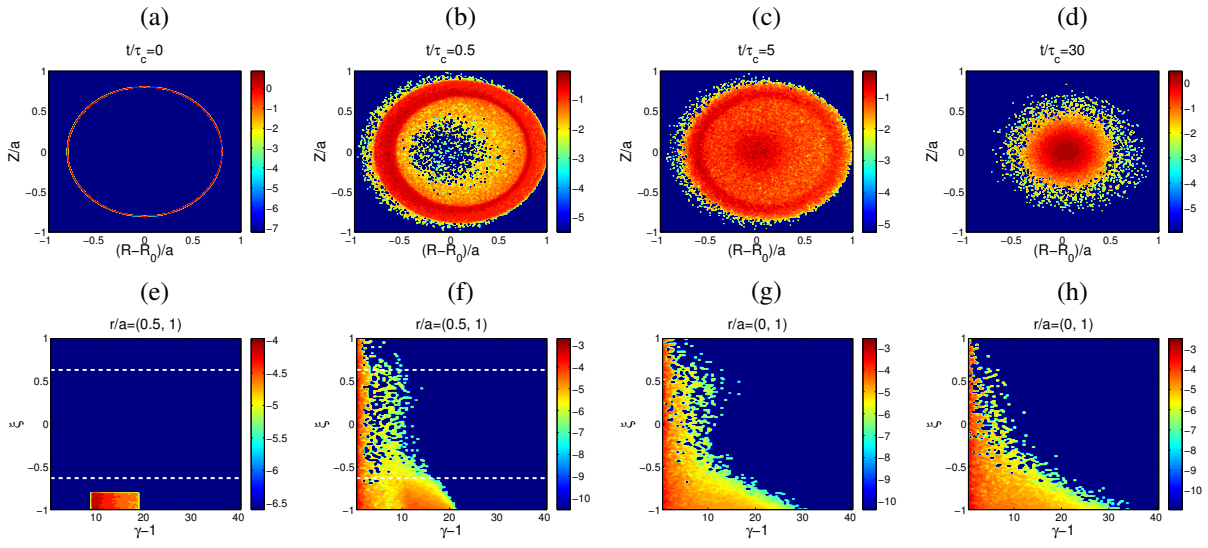

Figure 9. Time slices of the spatial and momentum space distribution. The top row displays the spatial profile of runaway electrons whereas the bottom row displays the momentum space profile. All momentum space plots only include electrons on the weak field side, where the dashed lines (when present) indicate the location of the trapped-passing boundary. The parameters were taken to be $E/E_c = 17$, $\bar{\alpha} = 0.05$, $T_e = 2$ eV, $\ln\Lambda_0 = 10$, $q_0 = 2.1$, $q_2 = 2$, $c\tau_c/a = 5\times10^5$, $a = 60$ cm, $B_0 = 1.5$ T. The argon was assumed to be singly ionized with $n^+_{Ar} = n_D$.

time scale for the eigenmode. Defining the width of the eigenmode by

$$w_{RA}(t) \equiv \frac{4\pi^2 R_0}{N_{RA}} \int_0^a dr r^2 n_{RA}(r,t)\,, \tag{9}$$

where n_{RA} is the flux surface averaged runaway density. For a small inverse aspect ratio plasma, the total number of runaway electrons can be written as

$$N_{RA} \equiv 4\pi^2 R_0 \int_0^a dr r n_{RA}(r,t)\,. \tag{10}$$

Figure (10) shows the evolution of the eigenmode width for different magnetic field strengths. Our motivation for varying the magnetic field strength is that both the collisional diffusivity and the convection term scale with powers of the parameter $(c/a\omega_{ce}) \propto 1/aB_0$, which varies inversely with the magnetic field strength. Thus, this B_0 scan will directly probe the impact of transport on the structure of the runaway eigenmode. Here, it is apparent that as the magnetic field is increased the saturated mode width $w_{RA}(t_f)$ decreases, where t_f is the final time of the simulation. This is made more evident in Fig. 11, where the saturated mode width is plotted as a function of the magnetic field strength. A clear scaling with the inverse square root of the magnetic field strength

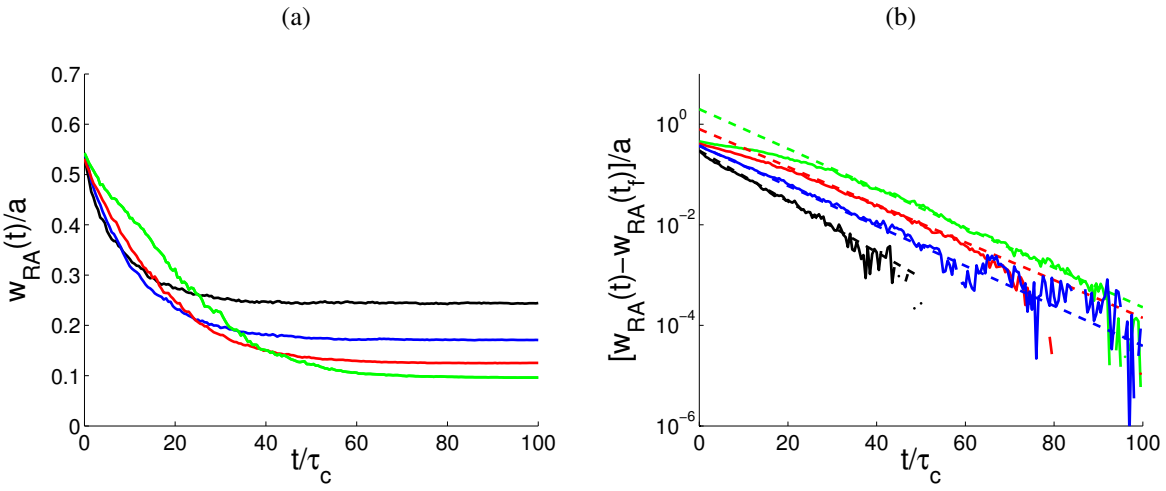

Figure 10. (a) Width of the runaway distribution versus time for different magnetic field strengths: $B_0 = 1$ T (black curve), $B_0 = 2$ T (blue curve), $B_0 = 4$ T (red curve), and $B_0 = 8$ T (green curve). (b) Same data as the left panel but subtracting off the saturated mode width $w_{RA}(t_f)$. The dashed curves correspond to exponential fits. The parameters were taken to be $E/E_c = 17.5$, $\bar{\alpha} = 0.05$, $T_e = 2$ eV, $\ln\Lambda_0 = 10$, $q_0 = 2.1$, $q_2 = 2$, $c\tau_c/a = 5 \times 10^5$, and $a = 60$ cm. The argon was assumed to be singly ionized with $n_{Ar}^+ = n_D$.

$\propto B_0^{-1/2}$ is evident. Such a scaling suggests that the saturated eigenmode width is not determined by the finite orbit width of the runaway electrons for this parameter range, since the width of the electron's orbit scales as $\propto 1/B_0$.

We note that since the parameter $\bar{\alpha} \equiv \tau_c/\tau_s \propto B_0^2/n_e$ varies strongly as the strength of the magnetic field is scanned, a fully self-consistent B_0 scan would result in $\bar{\alpha}$ also being varied. We have, however, elected to keep $\bar{\alpha}$ constant in order to isolate the impact of varying the quantity $c/a\omega_{ce} \propto 1/aB_0$, while keeping all other quantities constant. Such a procedure has the effect that the local avalanche growth rate and threshold remain approximately invariant, while the relative size of the runaway electron's orbit width is varied.

An additional observation evident from the right panel of Fig. 10 is that after a brief transient the width of the runaway electron distribution converges exponentially to the saturated mode width. The rate of the exponential convergence can be used to define the runaway relaxation time scale τ_{RA} by assuming a form

$$w_{RA}(t) - w_{RA}(t_f) \propto \exp(-t/\tau_{RA}). \tag{11}$$

The fitted curves and relaxation times are indicated in Figs. 10(b) and 11(b). We note that while

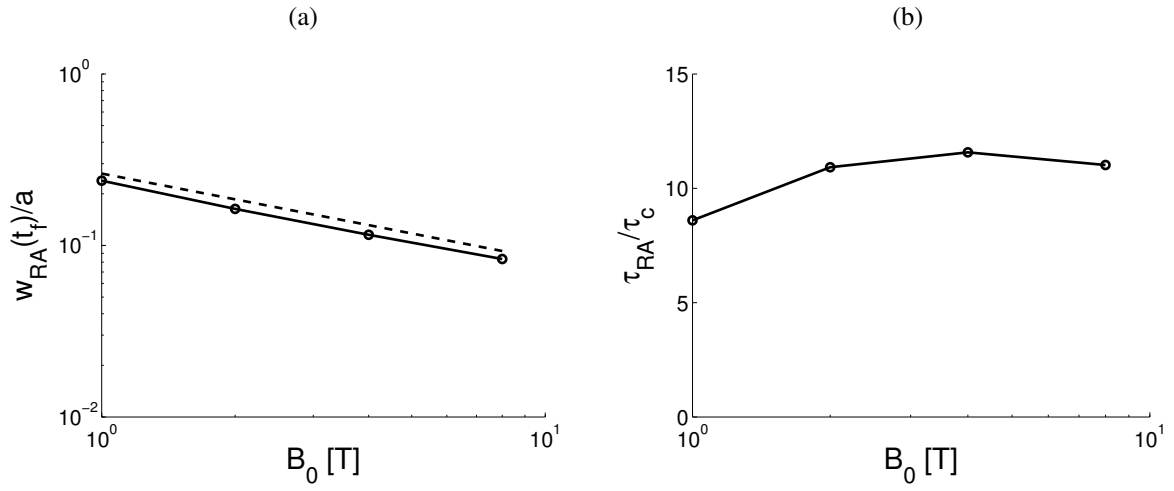

Figure 11. (left) Log-log plot of the saturated mode width (solid black curve) as a function of the magnetic field strength. The dashed curve indicates a curve scaling with $\propto B_0^{-1/2}$. (right) Estimated runaway relaxation time τ_{RA} versus B_0. The parameters are the same as Fig. 10.

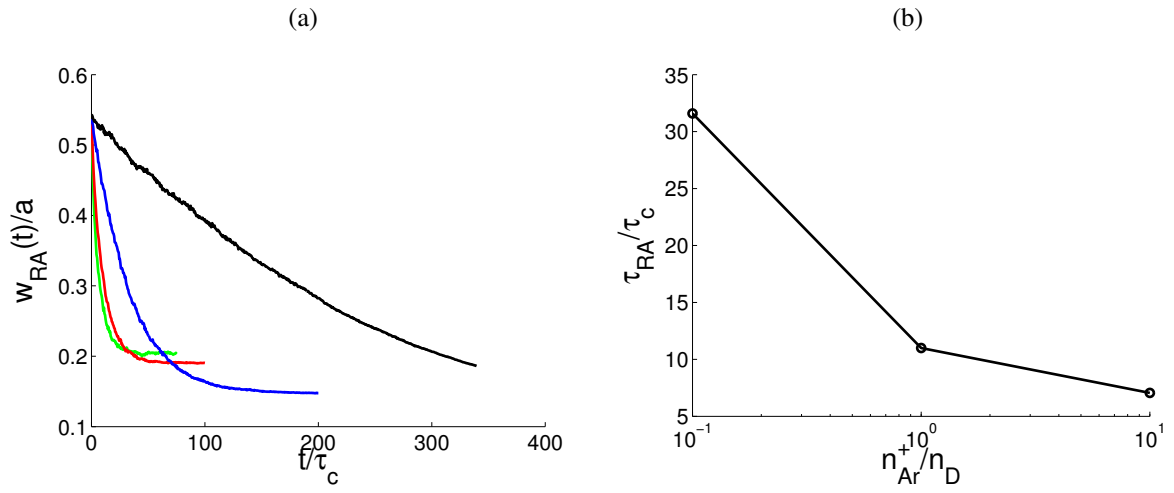

Figure 12. (a) Width of the runaway distribution versus time for different impurity fractions: $n^+_{Ar}/n_D = 0.01$ (black curve), $n^+_{Ar}/n_D = 0.1$ (blue curve), $n^+_{Ar}/n_D = 1$ (red curve), and $n^+_{Ar}/n_D = 10$ (green curve). (b) Runaway electron relaxation time τ_{RA} as a function of the impurity fraction. The parameters were taken to be $\bar{\alpha} = 0.05$, $T_e = 2$ eV, $\ln \Lambda_0 = 10$, $q_0 = 2.1$, $q_2 = 2$, $c\tau_c/a = 5 \times 10^5$, $a = 60$ cm, and $B_0 = 1.5$ T. The electric field was adjusted to put the system slightly above mariginality for all cases.

τ_{RA} tends to increase for larger B_0, the dependence is very weak. In addition, due to the discrete particle noise present in the simulations, once the eigenmode width is within $\sim 10^{-3}$ of its saturated mode width, the quantity $w_{RA}(t) - w_{RA}(t_f)$ becomes noisy [see Fig. 10(b)]. This limits the accuracy of the fitted value of τ_{RA}. A much stronger variation of τ_{RA} can be obtained by varying

the impurity fraction. As discussed in Sec. III above, an increase in the impurity content increases both the diffusive and convective transport. An increase to these transport processes will impact the eigenmode width as well as the time required to access the runaway eigenmode. Such a scan is shown in Fig. 12. Here it is apparent that as the impurity fraction is increased the saturated mode width increases, whereas the runaway relaxation time decreases drastically. The former trend largely results from the stronger spatial diffusion broadening the eigenmode's width. The latter trend is made more evident in Fig. 12(b), where the runaway relaxation time increases precipitously as the argon fraction is reduced. Such a trend implies that runaway electrons are unlikely to reach their asymptotic spatial distribution for a fully ionized low-Z plasma during experimentally relevant time scales. Indeed, for the case of a trace impurity fraction ($n_{Ar}^{+} = n_D/100$), the eigenmode width has not saturated to its asymptotic value after $> 300\tau_c$. In contrast, the presence of impurities reduces both the relativistic collision time τ_c (since the free electron density is typically increased compared to its pre-disruption value [32]), and the number of collision times τ_c required to relax to the saturated eigenmode width. Thus, runaway electrons will be far more likely to approach their asymptotic width in this latter case.

V. CONCLUSIONS

The principal conclusions of this work can be delineated as follows.

1. While the collisional transport of runaway electrons has been found to be weak in fully ionized low-Z plasmas, the presence of a significant fraction of partially ionized high-Z impurities has been shown to substantially increase both the collisional diffusivity and the inward convective transport of runaway electrons.

2. The enhancement of the spatial transport of runaway electrons, particularly the inward convective flow due to the Ware pinch, allows for the establishment of a global runaway eigenmode. For small to mid size tokamaks, the transport is shown to be sufficiently strong such that the system relaxes to a global runaway eigenmode nearly irrespective of the spatial distribution of the seed runaway population. This result suggests that plasmas under these conditions cannot be adequately described on a flux surface by flux surface basis.

3. The saturated width and relaxation time of the runaway eigenmode are computed for various plasma conditions. It was found that the width of the runaway eigenmode scales inversely

with the strength of the magnetic field, and that the presence of impurities strongly reduces the runaway relaxation time into their spatial eigenmode and increases the eigenmode width.

The importance of spatial transport in an axisymmetric plasma depends sensitively on the device size relative to the orbit width of the runaway electron which may be parameterized by the quantity $(c/a\omega_{ce}) \propto 1/aB_0$. Specifically, the collisional diffusivity scales quadratically with $(c/a\omega_{ce})$ whereas the Ware pinch scales linearly with $(c/a\omega_{ce})$. Spatial transport in axisymmetric configurations will thus tend to be most important in small to mid size devices, and become progressively weaker in larger tokamaks. This is made evident in the avalanche growth rate calculation of Fig. 1, where an exceptionally large magnetic field was introduced in order to allow the avalanche growth rate to be computed on a flux surface by flux surface basis. Such a modest level of transport for large devices also implies a greater degree of sensitivity to the spatial profile of the seed runaway population. As evident from the large magnetic field cases shown in Figs. 10 and 11, however, the spatial eigenmode is still accessable, albeit on a somewhat longer timescale. In contrast, for a mid size tokamak with a large impurity content, a flux surface by flux surface calculation of the avalanche growth rate is no longer possible due to the presence of strong spatial transport. This latter point is highlighted in the example case shown in Fig. 9. Here, the Ware pinch allowed a seed population of energetic electrons to be transported from the tokamak edge to the tokamak core, resulting in the establishment of the runaway global eigenmode.

ACKNOWLEDGMENTS

This work was jointly supported by the Theory Program of Office of Fusion Energy Sciences, and two SciDAC projects on Tokamak Disruption Simulation (TDS) and runaway electrons (SCREAM) by Office of Fusion Energy Science and Office of Advanced Scientific Computing.

Appendix A: Monte Carlo Estimation of Transport Coefficients

The convective and diffusive contributions will be estimated by noting

$$V(r) = \frac{d}{dt}\langle \Delta r(t) \rangle . \tag{A1}$$

$$D(r) = \frac{1}{2}\frac{d}{dt}\left[\left\langle \Delta r^2(t) \right\rangle - \langle \Delta r(t) \rangle^2\right] . \tag{A2}$$

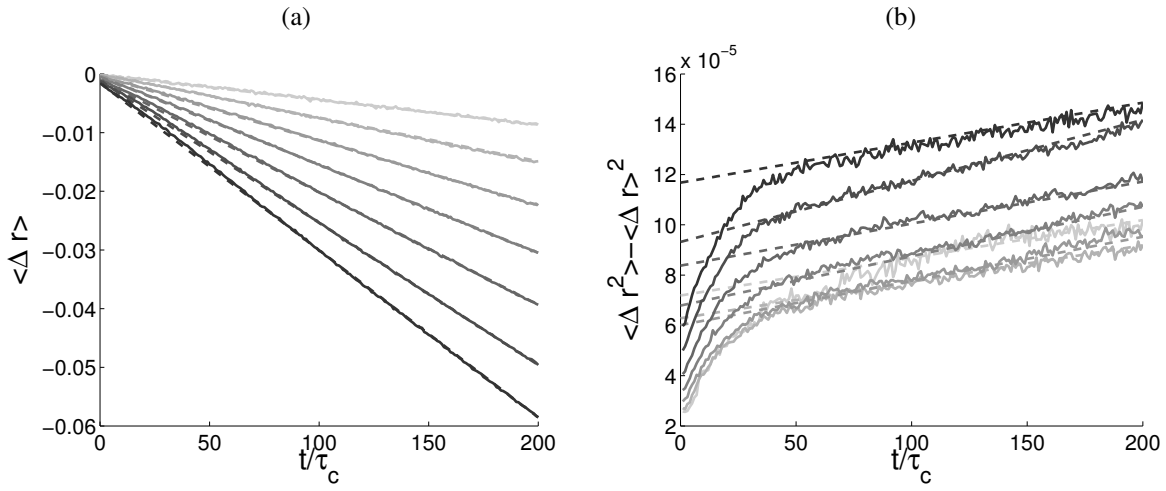

Figure 13. (a) Evolution of $\langle \Delta r \rangle$. (b) Evolution of $\langle \Delta r^2 \rangle - \langle \Delta r \rangle^2$. The shading of the curves become darker as the radius is increased. Approximately thirty eight thousand particles were initialized in the simulation. The solid lines are the data from the simulations whereas the dashed curves are fits used to estimate the transport coefficients. The other parameters were taken to be $a/R_0 = 1/3$, $(c\tau_c/a) = 5 \times 10^5$, $\bar{E}_1 = 3.5$, $\bar{\alpha} = 0.1$, $Z_{eff} = 5$, $v_{Te}/c = 0.0063$, $q_0 = 2.1$, $q_2 = 2$ and we considered an ITER like case ($a = 200$ cm, $B = 5.3$ T). The particles were initialized with $r/a = (0, 0.8)$.

Here, the average values $\langle \Delta r\,(t) \rangle$ and $\langle \Delta r^2\,(t) \rangle$ are computed by forming the quantity $\Delta r_i\,(t) \equiv r_i\,(t) - r_i\,(0)$ for each marker particle. A binning routine is then used based on the initial radial position of the marker particle in order to construct radially dependent average values of $\langle \Delta r\,(t) \rangle$ and $\langle \Delta r^2\,(t) \rangle$. Once these average quantities have been computed, the resulting convective and diffusion contributions to the particle transport can be computed from Eqs. (A1) and (A2). An example case is shown in Fig. 13.

[1] J. Decker, E. Hirvijoki, O. Embreus, Y. Peysson, A. Stahl, I. Pusztai, and T. Fülöp, Plasma Physics and Controlled Fusion **58**, 025016 (2016).

[2] Z. Guo, C. J. McDevitt, and X.-Z. Tang, Plasma Physics and Controlled Fusion **59**, 044003 (2017).

[3] P. Aleynikov and B. N. Breizman, Physical review letters **114**, 155001 (2015).

[4] C. J. McDevitt, Z. Guo, and X.-Z. Tang, Plasma Physics and Controlled Fusion **60**, 024004 (2018).

[5] P. Aleynikov and B. Breizman, Nuclear Fusion **55**, 043014 (2015).

[6] C. Liu, E. Hirvijoki, G.-Y. Fu, D. P. Brennan, A. Bhattacharjee, and C. Paz-Soldan, Phys. Rev. Lett. **120**, 265001 (2018), URL https://link.aps.org/doi/10.1103/PhysRevLett.120.265001.

[7] Z. Guo, C. J. McDevitt, and X.-Z. Tang, Physics of Plasmas **25**, 032504 (2018).

[8] G. Papp, M. Drevlak, T. Fülöp, and P. Helander, Nuclear Fusion **51**, 043004 (2011).

[9] V. Izzo, E. Hollmann, A. James, J. Yu, D. Humphreys, L. Lao, P. Parks, P. Sieck, J. Wesley, R. Granetz, et al., Nuclear Fusion **51**, 063032 (2011).

[10] C. Sommariva, E. Nardon, P. Beyer, M. Hoelzl, G. Huijsmans, D. van Vugt, and J. Contributors, Nuclear Fusion **58**, 016043 (2017).

[11] D. del Castillo-Negrete, L. Carbajal, D. Spong, and V. Izzo, Physics of Plasmas **25**, 056104 (2018).

[12] V. Izzo, D. Humphreys, and M. Kornbluth, Plasma Physics and Controlled Fusion **54**, 095002 (2012).

[13] T. Hender, J. Wesley, J. Bialek, A. Bondeson, A. Boozer, R. Buttery, A. Garofalo, T. Goodman, R. Granetz, Y. Gribov, et al., Nuclear fusion **47**, S128 (2007).

[14] B. Breizman and P. Aleynikov, Proceedings of the 26th IAEA International Conference, 17-22 October 2016, Kyoto, Japan, OV/2-3.

[15] L. Hesslow, O. Embréus, A. Stahl, T. C. DuBois, G. Papp, S. L. Newton, and T. Fülöp, Phys. Rev. Lett. **118**, 255001 (2017), URL https://link.aps.org/doi/10.1103/PhysRevLett.118.255001.

[16] L. Hesslow, O. Embréus, G. J. Wilkie, G. Papp, and T. Fülöp, arXiv preprint arXiv:1802.00717 (2018).

[17] A. Ware, Physical Review Letters **25**, 15 (1970).

[18] A. A. Galeev, Sov. Phys. JETP **32**, 752 (1971).

[19] A. K. Fontanilla and B. N. Breizman, Physics of Plasmas **24**, 112509 (2017).

[20] C. McDevitt, Z. Guo, and X.-Z. Tang, *Avalanche instability of runaway electrons under conditions typical of a disrupting tokamak plasma*, to be submitted to Plasma Physics and Controlled Fusion (2018).

[21] A. H. Boozer and G. Kuo-Petravic, The Physics of Fluids **24**, 851 (1981).

[22] P. Helander, M. Lisak, and D. Ryutov, Plasma physics and controlled fusion **35**, 363 (1993).

[23] A. H. Boozer, Physics of Plasmas **22**, 032504 (2015).

[24] C. Liu, D. P. Brennan, A. H. Boozer, and A. Bhattacharjee, Plasma Physics and Controlled Fusion **59**, 024003 (2017), URL http://stacks.iop.org/0741-3335/59/i=2/a=024003.

[25] O. Embréus, A. Stahl, and T. Fülöp, Journal of Plasma Physics **84** (2018).

[26] H. Smith, P. Helander, L.-G. Eriksson, D. Anderson, M. Lisak, and F. Andersson, Physics of plasmas **13**, 102502 (2006).

[27] A. Rechester and M. Rosenbluth, Physical Review Letters **40**, 38 (1978).

[28] M. Rosenbluth, R. Hazeltine, and F. L. Hinton, The Physics of Fluids **15**, 116 (1972).

[29] J. Connor and R. Hastie, Nuclear fusion **15**, 415 (1975).

[30] X. Guan, H. Qin, and N. J. Fisch, Physics of Plasmas **17**, 092502 (2010).

[31] D. Hu and H. Qin, Physics of Plasmas **23**, 032510 (2016).

[32] E. Hollmann, M. Austin, J. Boedo, N. Brooks, N. Commaux, N. Eidietis, D. Humphreys, V. Izzo, A. James, T. Jernigan, et al., Nuclear Fusion **53**, 083004 (2013).